# Hybrid Noise Removal in Hyperspectral Imagery With a Spatial–Spectral Gradient Network

Qiang Zhang, *Student Member, IEEE*, Qiangqiang Yuan, *Member, IEEE*, Jie Li, *Member, IEEE*, Xinxin Liu, Huanfeng Shen, *Senior Member, IEEE*, and Liangpei Zhang, *Fellow, IEEE*

***Abstract*— The existence of hybrid noise in hyperspectral images (HSIs) severely degrades the data quality, reduces the interpretation accuracy of HSIs, and restricts the subsequent HSI applications. In this paper, the spatial–spectral gradient network (SSGN) is presented for mixed noise removal in HSIs. The proposed method employs a spatial–spectral gradient learning strategy, in consideration of the unique spatial structure directionality of sparse noise and spectral differences with additional complementary information for effectively extracting intrinsic and deep features of HSIs. Based on a fully cascaded multiscale convolutional network, SSGN can simultaneously deal with different types of noise in different HSIs or spectra by the use of the same model. The simulated and real-data experiments undertaken in this study confirmed that the proposed SSGN outperforms at mixed noise removal compared with the other state-of-the-art HSI denoising algorithms, in evaluation indices, visual assessments, and time consumption.**

***Index Terms*— Gradient learning, hybrid noise, hyperspectral, multiscale convolutional network, spatial–spectral.**

## I. Introduction

DUE to the abundant spectral information, hyperspectral image (HSI) data [1] have been successfully applied in ground object classification [2], endmember extraction [3], and unmixing [4]. Nevertheless, because of the sensor instability and atmospheric interference, HSIs often suffer from multiple types of noise [5], such as Gaussian noise, stripe noise, impulse noise, dead lines, and mixed noise, as illustrated in Fig. 1. The degraded information often disturbs and limits subsequent processing. Therefore, noise reduction in HSIs is crucial before image interpretation and the subsequent applications [6], [7].

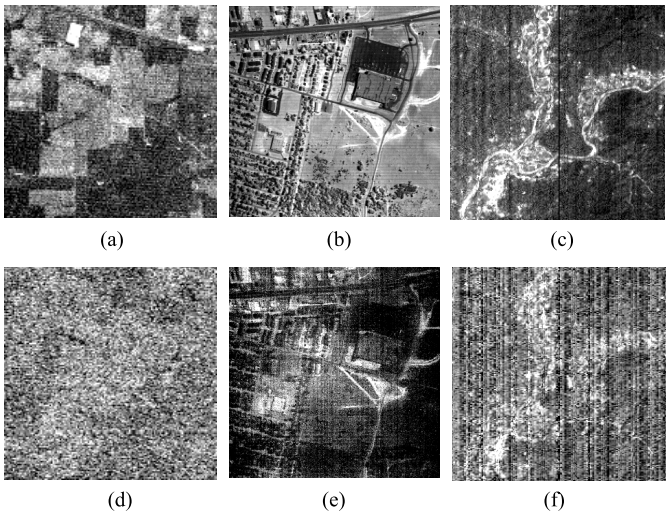


Fig. 1. Multiple types and levels of noise in different HSIs and different bands. (a) Indian Pines image band 2. (b) AVIRIS Urban image band 103. (c) EO-1 Hyperion image band 2. (d) Indian Pines image band 109. (e) AVIRIS Urban image band 104. (f) EO-1 Hyperion image band 166.

To date, by treating the HSI as 3-D cube data, many different algorithms [8]–[17] have been proposed for HSI denoising. Details of the main HSI denoising methods are provided in Section II. Although the existing HSI denoising methods can obtain favorable outcomes, there are still several challenges and bottlenecks that need to be solved. First, the manual parameters must be adjusted suitably and carefully for different HSI data, which brings about inconvenient, nonuniversal, and time-consuming drawbacks for different scenarios and HSI sensors. Second, the noise in HSIs exists in both the spatial and spectral domains, with various types and diverse levels, as displayed in Fig. 1. However, most algorithms are unable to satisfy the complex situation of mixed noise. As a result, the processed data often contain residual noise or show spectral distortion. Third, most bands in HSIs are of high quality, while only some specific bands are degraded by diverse noise. Therefore, how to effectively reduce the

Manuscript received January 14, 2019; revised March 15, 2019; accepted March 26, 2019. Date of publication June 11, 2019; date of current version September 25, 2019. This work was supported in part by the National Key Research and Development Program of China under Grant 2016YFC0200900 and Grant 2016YFB0501403, in part by the National Natural Science Foundation of China under Grant 41701400, in part by the Fundamental Research Funds for the Central Universities under Grant 2042017kf0180 and Grant 531118010209, and in part by the Natural Science Foundation of Hubei Province under Grant ZRMS2017000729. *(Corresponding author: Jie Li.)*

Q. Zhang is with the State Key Laboratory of Information Engineering in Surveying, Mapping and Remote Sensing, Wuhan University, Wuhan 430079, China (e-mail: whuqzhang@gmail.com).

Q. Yuan is with the School of Geodesy and Geomatics, Wuhan University, Wuhan 430079, China, and also with the Collaborative Innovation Center of Geospatial Technology, Wuhan University, Wuhan 430079, China (e-mail: qqyuan@sgg.whu.edu.cn).

J. Li is with the School of Geodesy and Geomatics, Wuhan University, Wuhan 430079, China (e-mail: aaronleecool@whu.edu.cn).

X. Liu is with the College of Electrical and Information Engineering, Hunan University, Changsha 410082, China (e-mail: liuxinxin@hnu.edu.cn).

H. Shen is with the School of Resource and Environmental Science, Wuhan University, Wuhan 430079, China, and also with the Collaborative Innovation Center of Geospatial Technology, Wuhan University, Wuhan 430079, China (e-mail: shenhf@whu.edu.cn).

L. Zhang is with the State Key Laboratory of Information Engineering in Surveying, Mapping and Remote Sensing, Wuhan University, Wuhan 430079, China, and also with the Collaborative Innovation Center of Geospatial Technology, Wuhan University, Wuhan 430079, China (e-mail: zlp62@whu.edu.cn).

Color versions of one or more of the figures in this article are available online at http://ieeexplore.ieee.org.

Digital Object Identifier 10.1109/TGRS.2019.2912909

noise in the corrupted bands while simultaneously preserving the high-quality bands is of great importance for HSI denoising. Overall, there is a need to establish a convenient, universal, efficient, and robust denoising framework that can adapt to different HSI data with different and mixed noise types.

Recently, on account of the powerful feature extraction and nonlinear expression ability brought by deep learning like deep convolutional neural networks (DCNNs) [18], [19], many low-level vision problems [20]–[23] in remote sensing data, such as synthetic aperture radar (SAR) image despeckling [20], pansharpening [21], [22], and missing data reconstruction [23], have been provided with a learning framework which can achieve the state-of-the-art performance. To overcome the drawbacks mentioned above for HSIs denoising and take full advantage of DCNNs, we propose a spatial–spectral gradient network (SSGN) for hybrid noise reduction in HSIs considering the noise type of Gaussian noise, stripe noise, impulse noise, dead line, and their mixture. The main innovations can be generalized as follows.

1) A spatial–spectral convolutional network is proposed for HSI denoising. To take the advantage of the abundant spectral information in HSIs and the distinct spatial information for each band, SSGN simultaneously employs the spatial data and the adjacent spectral data in fully cascaded multiscale convolutional neural network blocks.
2) The spatial gradient and spectral gradient are jointly incorporated in the proposed model. The spatial gradient is utilized to extract the unique structure directionality of sparse noise in the horizontal and vertical directions, and the spectral gradient is used to obtain spectral additional complementary information for the noise removal. The spectral gradient is also integrated into the spatial–spectral loss function to reduce the spectral distortion in the whole framework.
3) The experimental results confirm that the proposed method can effectively deal with the Gaussian noise, stripe noise, and mixed noise in different HSIs or spectra through a single model. Compared with the other state-of-the-art HSI denoising algorithms, SSGN outperforms in evaluation indices, visual assessments, and time consumption under different mixed noise scenarios.

The rest of this paper is organized as follows. Section II describes the HSI degradation procedure caused by hybrid noise, and then introduces the existing HSI denoising methods. In Section III, the proposed model is described. The simulated and real-data experimental results are presented in Section IV. Finally, our conclusions are given in Section V.

## II. Related Work

Given an HSI is a 3-D tensor $\mathbf{Y} \in \mathbb{R}^{M\times N\times B}$, where $M$ and $N$ represent the spatial dimension and $B$ denotes the spectral dimension, the HSI noise degradation model can be described as [24]

$$\mathbf{Y} = \mathbf{X} + \mathbf{D} + \mathbf{S} \tag{1}$$

where $\mathbf{X} \in \mathbb{R}^{M\times N\times B}$ represents the clean HSI data, $\mathbf{D} \in \mathbb{R}^{M\times N\times B}$ denotes the dense noise such as Gaussian noise, and $\mathbf{S} \in \mathbb{R}^{M\times N\times B}$ denotes the sparse noise such as sparse-distributed stripe noise and dead lines. To obtain noise-free data $\mathbf{X}$ from (1) with only $\mathbf{Y}$ known, many scholars have developed different models for the HSI denoising problem. The existing HSI denoising methods can be roughly classified into two types [26]: 1) filter-based methods and 2) model optimization-based methods. The specific peculiarities, advantages, and disadvantages of these two types of methods are described as follows.

### A. Filter-Based Methods

The filter-based methods aim to separate clean signals from the noisy signals through filtering operations, such as Fourier transform, wavelet transform, or a nonlocal means (NLM) filter. For example, Othman and Qian [8] proposed a combined spatial–spectral derivative-domain wavelet shrinkage noise removal method. This method depends on the spectral derivative domain and benefits from the dissimilarity of the signal nature in the spatial and spectral dimensions, where the noise level is elevated. In addition, based on the NLM strategy, Maggioni *et al.* [9] presented an extension of the block-matching and 3-D filtering (BM3-D) [27] algorithm from 2-D data to a 3-D data cube, employing principal component analysis (PCA) and 3-D transform for the noise reduction. The major drawback of these filtering methods lies in the usage of the handcrafted and fixed wavelet, which are sensitive to the selection of the transform function and cannot consider the differences in the geometrical characteristics of HSIs such as mixed noise.

### B. Model Optimization-Based Methods

The model optimization-based methods, such as total variation [10], sparse representation [11], [12], and low-rank matrix and tensor models [13]–[17], take the reasonable assumption or priors of the HSI data into account. This type of method can map the noisy HSI to the clear one in an attempt to preserve the spatial and spectral characteristics. For example, considering the noise intensity difference in different bands, Yuan *et al.* [10] proposed a spatial–spectral adaptive total variation denoising algorithm. Furthermore, by applying the sparsity prior of the HSI data, Zhao and Yang [11] investigated the sparse coding to describe the global redundancy and correlation (RAC) and the local RAC in the spectral domain and then employed a low-rank constraint to capture the global RAC in the spectral domain. Furthermore, Li *et al.* [12] exploited the intraband structure and the interband correlation in the process of joint sparse representation and joint dictionary learning.

For an HSI, both the high spectral correlation between adjacent bands and the high spatial similarity within one band can reveal the low-rank property [13], [14] or tensor [15]–[17] structure of the HSI. Hence, by lexicographically transforming a 3-D cube into a 2-D matrix representation along the spectral dimension, Zhang *et al.* [13] and He *et al.* [14] proposed a low-rank matrix restoration model for the mixed noise removal in HSIs. Recently, to adequately utilize the spectral–spatial

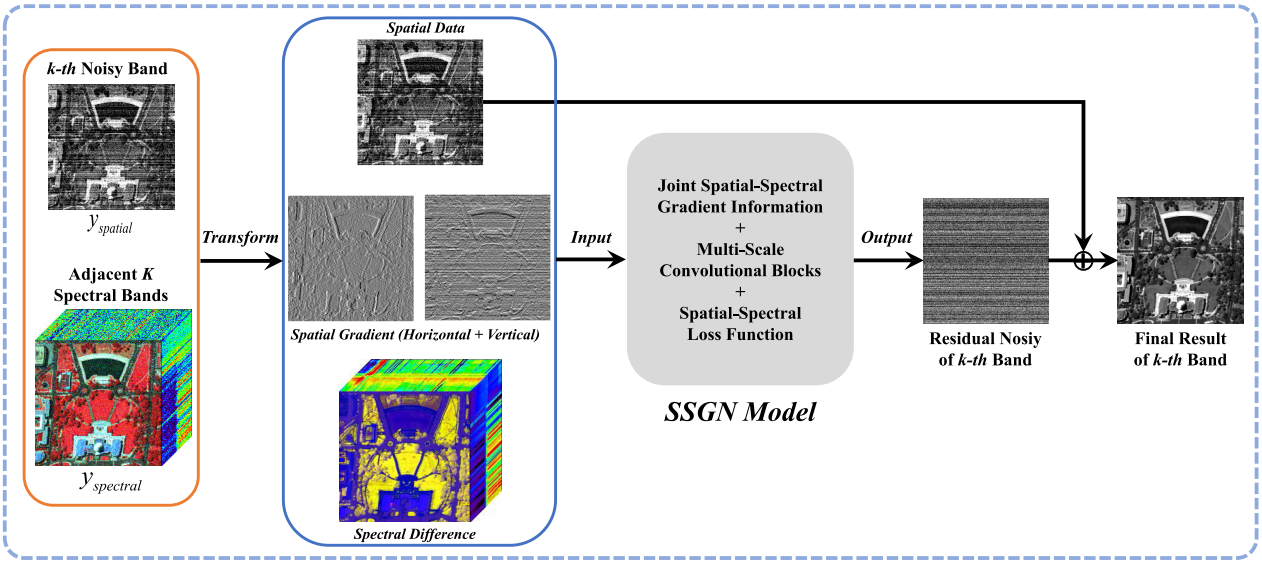


Fig. 2. Flowchart of the HSI denoising procedure with the proposed method.

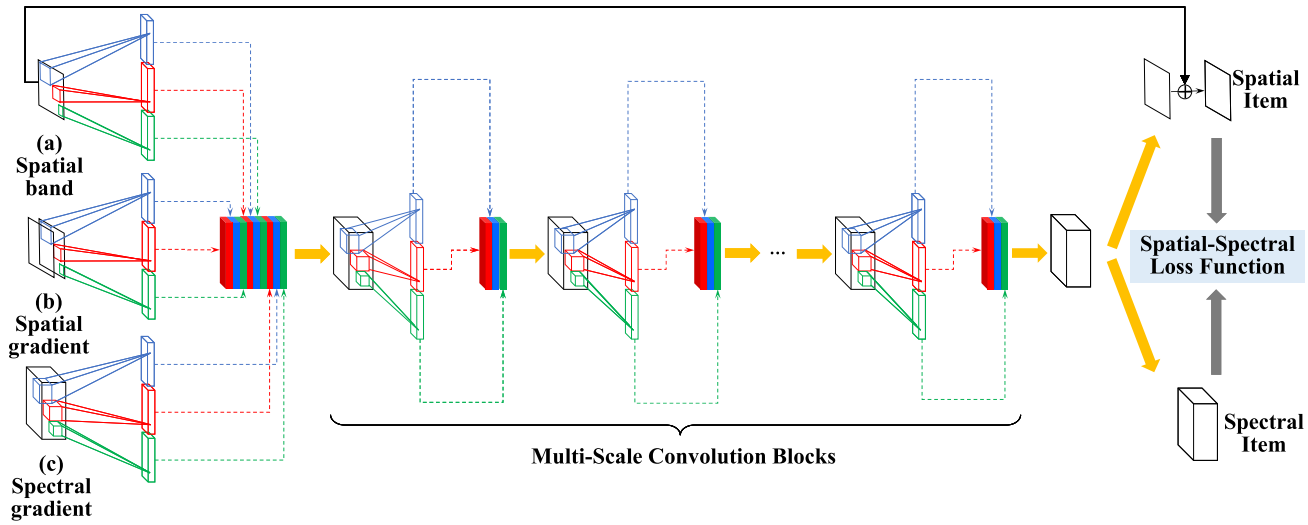


Fig. 3. Proposed SSGN model.

structural property for the 3-D tensor HSIs, low-rank tensor-based HSI denoising methods [15]–[17] have been proposed and have achieved the state-of-the-art performances, at the cost of higher computation time consumption.

In summary, although the existing HSI denoising methods can obtain favorable results, the inadaptability for hybrid noise removal in different HSIs and the low-efficiency issue still restrict the application of HSI denoising. Therefore, to overcome the deficiency of the above-mentioned methods to some degree and take the full advantage of a DCNN in remote sensing data [28]–[30], we present the SSGN model for efficient hybrid noise reduction in HSIs.

## III. Methodology

### A. Holistic Framework Description

To remove the diverse types of noise in HSIs, the proposed SSGN method takes the noise structure characteristic, the spatial peculiarity for each band, and the spectral redundancy into account. Through learning in an end-to-end fashion between a noisy HSI patch and a clean HSI patch, we present the SSGN model for HSI hybrid noise reduction. The SSGN model simultaneously employs the simulated $k$th noisy band, its horizontal/vertical spatial gradient, and its adjacent spectral gradient as the input data, which outputs the residual noise of the $k$th noisy band. Then, by traversing all the bands of the HSI in this way, we can finally obtain the denoising results for all the bands. The flowchart of the HSI denoising procedure with the SSGN model is depicted in Fig. 2. Specific details of the proposed SSGN model are provided in Section III-B.

### B. Proposed SSGN Model for HSI Denoising

Fig. 3 illustrates the architecture of the proposed SSGN model. The input spatial band represents the current noisy band in the top-left corner. The spatial gradient in the middle-left corner denotes the vertical and horizontal gradient of the input spatial band. Correspondingly, the input spectral gradient represents the adjacent spectral difference cube with the current spatial noisy band in the bottom-left corner. Based on an

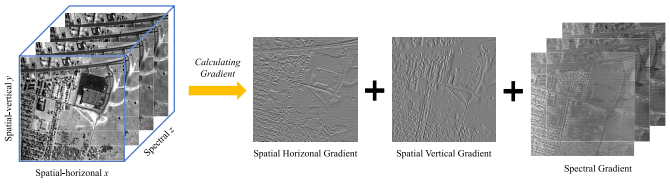


Fig. 4. Spatial and spectral gradient results in the HSI.

end-to-end framework with fully cascaded multiscale convolutional blocks, the proposed SSGN employs a spatial–spectral loss function to optimize the model's trainable parameters. The proposed method then traverses all the spatial bands and their adjacent spectral bands in the HSI, which simultaneously utilizes the spatial–spectral gradient information for HSI denoising.

*1) Joint Spatial and Spectral Gradient Information:* To some extent, the gradient information of the spatial band can effectively highlight the sparse noise, especially sparse-distributed stripe noise, because of its unique structure directionality, as shown in Fig. 4. Furthermore, as HSI data contain abundant spectral information with hundreds of bands, the noise levels and types in each band are usually different. These differences in HSIs provide additional complementary information, which can be beneficial to remove mixed noise for HSIs. From the above, we argue that mixed noise in HSIs, including dense noise and spare noise, can be removed from both the spatial and spectral domains by employing joint spatial and spectral gradient information, as follows:

$$\mathbf{G}_x(m,n,k) = \mathbf{Y}(m+1,n,k) - \mathbf{Y}(m,n,k) \tag{2}$$

$$\mathbf{G}_y(m,n,k) = \mathbf{Y}(m,n+1,k) - \mathbf{Y}(m,n,k) \tag{3}$$

$$\mathbf{G}_z(m,n,k) = \mathbf{Y}(m,n,k+1) - \mathbf{Y}(m,n,k) \tag{4}$$

where $\mathbf{G}_x$, $\mathbf{G}_y$, and $\mathbf{G}_z$ stand for the horizontal spatial gradient, the vertical spatial gradient, and the spectral gradient of the current band $\mathbf{Y}_k$, respectively. For the $k$th band in the HSI, $\mathbf{G}_z$ represents its adjacent bands with the number $K$. Instead of directly generating the final denoising results, a residual learning strategy is utilized to estimate the noise elements, which can also ensure the stability and efficiency of the training procedure in the proposed SSGN model [31]–[33]. The final reconstruction output of the $k$th band is denoted as

$$\hat{\mathbf{X}}_k = \mathbf{F}_l \circ \cdots \circ \mathbf{F}_2 \circ \mathbf{F}_1\{\mathbf{Y}_k, \mathbf{G}_x, \mathbf{G}_y, \mathbf{G}_z\} + \mathbf{Y}_k \tag{5}$$

where $\mathbf{F}_l$ represents the $l$th multiscale convolutional block operation of the proposed model, $\circ$ stands for the feature map transformation from $\mathbf{F}_{l-1}$ to $\mathbf{F}_l$, and $\hat{\mathbf{X}}_k$ represents the estimated denoising result of the $k$th band. The multiscale convolutional blocks are introduced in detail below.

*2) Multiscale Convolutional Blocks:* In HSI data, as shown in Fig. 5(a), the feature expression may count on contextual information in different scales, since ground objects usually have multiplicative sizes in different nonlocal regions. Furthermore, multiscale convolutional filters can simultaneously obtain diverse receptive field sizes, especially for the scenario with stripe noise and dead lines, as displayed in Fig. 5(b).

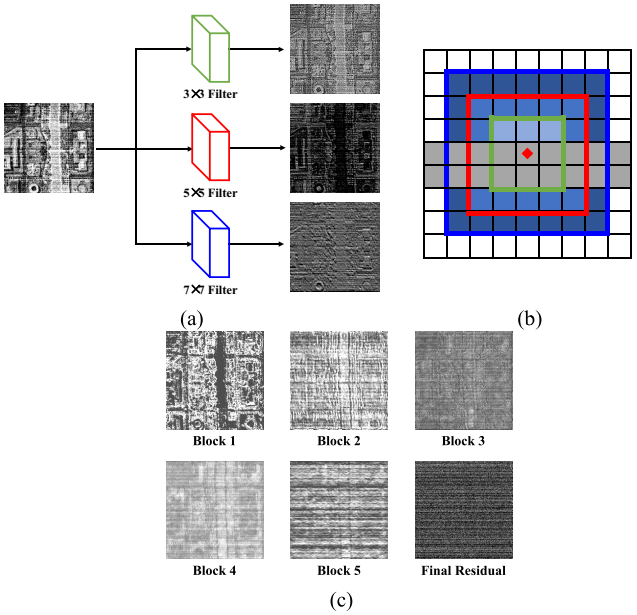


Fig. 5. (a) Multiscale convolutional block in Fig. 2. (b) Receptive field with sparse noise, such as sparse-distributed stripes or dead lines. (c) Feature maps through different cascaded blocks.

From this perspective, to effectively eliminate sparsely distributed noise such as stripe noise and dead lines in HSIs, the proposed SSGN model introduces multiscale convolutional blocks to extract multiscale features for the multicontext information. In addition, to capture both the multiscale spatial feature and spectral feature in HSIs, the proposed method employs different convolutional kernel sizes, as described in Fig. 5. The multiscale convolutional blocks contain three convolution operations of $3 \times 3$(green), $5 \times 5$(red), and $7 \times 7$ (blue) kernel sizes for the spatial data and spectral data, respectively. All these three convolutions for the current spatial band, spatial gradient, and corresponding spectral gradient produce feature maps of 30 channels, as revealed in Fig. 3(a)–(c), respectively.

In addition, the proposed SSGN also employs fully cascaded multiscale convolutional blocks for extracting more feature maps with different receptive field sizes. As shown in Fig. 5(c), as the depth of the layers increases, the results of different blocks gradually approximate to the final residual mixed noise, including dense noise such as Gaussian noise and sparse noise such as sparse-distributed stripe noise and dead lines.

*3) Spatial–Spectral Loss Function:* Loss functions form an indispensable module in the supervised learning procedure. To optimize the model parameters, the spatial–spectral loss function in the proposed SSGN method is utilized in the training process with a back-propagation algorithm. The traditional image restoration tasks, such as super-resolution and denoising, usually utilize a Euclidean loss function, which only considers the spatial information restoration and not the spectral information. Meanwhile, in HSI restoration, spectral preservation must be considered, which is crucial for the subsequent applications such as unmixing. Therefore, to simultaneously maintain the spatial structure information and restrain the spectral distortion, the proposed method

develops a spatial–spectral loss function during the training procedure, as follows:

$$\xi(\Theta) = (1-\alpha)\cdot \xi_{\text{spatial}} + \alpha \cdot \xi_{\text{spectral}} \tag{6}$$

where $\xi_{\text{spatial}}$ (spatial term) and $\xi_{\text{spectral}}$ (spectral term) are, respectively, defined as

$$\xi_{\text{spatial}} = \frac{1}{2T}\sum_{i=1}^{T} \left\| \mathbf{Res}_k^i - (\mathbf{Y}_k^i - \mathbf{X}_k^i) \right\|_2^2 \tag{7}$$

$$\xi_{\text{spectral}} = \frac{1}{2T}\sum_{i=1}^{T} \sum_{z=k-\frac{K}{2}, z\neq k}^{k+\frac{K}{2}} \left\| \Phi_z^i - \mathbf{G}_z^i \right\|_2^2 \tag{8}$$

where $\alpha$ is the penalty parameter for the tradeoff between the spatial and spectral items, $T$ stands for the number of training patches, $\mathbf{Res}_k$ is the estimated residual spatial output of the $k$th band, and $\Phi_z$ represents the estimated spectral gradient of bands $[k-(K/2):k-1, k+1:k+(K/2)]$. To sufficiently elaborate the effectiveness of the spatial–spectral loss function, a discussion is provided in Section IV-C.

## IV. Experiments and Discussion

To validate the effectiveness of the proposed SSGN for hybrid noise reduction in HSIs, both simulated and real noisy HSI data were employed. The proposed method was compared with the five existing state-of-the-art methods of hybrid spatial–spectral noise reduction (HSSNR) [8], block-matching and 4-D filtering (BM4-D) [9], low-rank matrix recovery (LRMR) [13], low-rank total variation (LRTV) [14], and nonconvex low-rank matrix approximation (NonLRMA) [34]. Before the denoising procedure, the gray values of each HSI band were independently all normalized to [0–1]. The mean peak signal-to-noise ratio (MPSNR) [35], the mean structural similarity index (MSSIM) [36], and the mean spectral angle (MSA) [37] were employed as assessment indices in the simulated experiments. Generally speaking, in simulated experiments, better HSI denoising effects can be reflected by higher MPSNR and MSSIM values and lower MSA values. For the real-data experiments, the three HSIs were tested and the reconstruction mean digital number (DN) results of all the rows or columns are displayed. The code of the proposed method can be downloaded from https://github.com/WHUQZhang.

1) *Parameter Settings*: The adjacent spectral band number was set as $K = 24$ and the tradeoff parameter was set as $\alpha = 0.001$ in the SSGN model for both the simulated and real-data experiments. Impact analysis for this parameter is provided in Section IV-C. The proposed SSGN model was trained with the Adam optimization algorithm [38] as the gradient descent optimization method, with momentum parameters of 0.9, 0.999, and $10^{-8}$, respectively. In addition, the learning rate was initialized to 0.001 for the whole network. After every ten epochs, the learning rate was decreased through being multiplied by a descent factor of 0.5.
2) *Network Training*: For the training of the proposed SSGN model, the University of Pavia image obtained by the airborne Reflective Optics System Imaging Spectrometer (ROSIS) sensor, with a size of $610 \times 340 \times 96$, and the Washington DC Mall image obtained by the Hyperspectral Digital Imagery Collection Experiment (HYDICE) airborne sensor, with a size of $1080 \times 303 \times 191$, were both employed as training data after removing the noisy and water absorption bands. These training labels were then cropped in each patch size as $25 \times 25$, with the sampling stride equaling to 25. The simulated mixed noise patch data were generated through imposing additive white Gaussian noise (AWGN), stripe noise, and dead lines on different spectra. The noise intensity and degree of distribution were also varied in different bands. Due to the fact that an increasing number of HSI training samples can effectively fit the HSI denoising model, multiangle image rotation (angles of 0, 90°, 180°, and 270° in our training data sets) and multiscale resizing (scales of 0.8, 1, 1.2, and 1.4 in our training data sets) were both utilized during the training procedure. The training process of SSGN took 200 epochs (an epoch is equal to about 1200 iterations). We employed the Caffe framework [39] to train the proposed model on a PC with Windows 7 environment, 16-GB RAM, an Intel Xeon E5-2609 v3 CPU, and an NVIDIA Titan X GPU. The training process for the proposed model costs roughly 13 h 45 min.
3) *Test Data Sets*: Four data sets were employed in the simulated and real-data experiments, as follows.
   a) The first data set was the Washington DC Mall image mentioned above in Section IV-B, which was cropped to $200 \times 200 \times 191$ for the simulated-data experiments, after removing the water absorption bands.
   b) The second data set was the HYDICE Urban HSI with a size of $307 \times 307 \times 188$, which was employed for the real-data experiments after removing the severely degraded bands.
   c) The third data set was the Airborne Visible Infrared Imaging Spectrometer (AVIRIS) Indian Pines HSI with a size of $145 \times 145$, which was employed for the real-data experiments. A total of 206 bands were utilized in the experiments after removing bands 150–163, which are severely disturbed by the atmosphere and water.
   d) The fourth data set was the EO-1 Hyperion data set with a size of $400 \times 200 \times 166$, which was employed for the real-data experiments after removing the water absorption bands.

### A. Simulated-Data Experiments

In the simulated HSI hybrid noise reduction process, the additional noise was simulated as the following five cases.

*Case* 1 *(Gaussian Noise)*: All bands in the HSIs were corrupted by Gaussian noise. For different spectra, the noise intensity was different and conformed to a random probability distribution [40].

TABLE I
QUANTITATIVE EVALUATION OF THE HYBRID NOISE REDUCTION RESULTS IN THE SIMULATED EXPERIMENTS

| | Noisy HSI | HSSNR | BM4D | LRMR | LRTV | NonLRMA | SSGN |
|---|---|---|---|---|---|---|---|
| ***Case 1: Gaussian noise*** | | | | | | | |
| MPSNR | 23.27 | 27.25 | 28.62 | 33.21 | 33.96 | 32.15 | **34.37** |
| MSSIM | 0.769 | 0.923 | 0.941 | 0.981 | 0.980 | 0.981 | **0.982** |
| MSA | 19.47 | 9.083 | 5.116 | 4.628 | 5.507 | 5.312 | **4.241** |
| Time/s | - | 304.4 | 461.8 | 449.6 | 175.1 | 548.4 | **7.3** |
| ***Case 2: Stripe noise*** | | | | | | | |
| MPSNR | 32.24 | 34.34 | 33.49 | 37.68 | 36.17 | 37.89 | **39.15** |
| MSSIM | 0.945 | 0.967 | 0.959 | 0.974 | 0.973 | 0.976 | **0.992** |
| MSA | 7.132 | 6.324 | 6.814 | 5.175 | 5.351 | 4.862 | **2.904** |
| Time/s | - | 319.7 | 445.8 | 527.4 | 169.9 | 610.7 | **7.5** |
| ***Case 3: Gaussian noise + stripe noise*** | | | | | | | |
| MPSNR | 21.66 | 26.08 | 28.24 | 31.27 | 31.74 | 31.28 | **33.18** |
| MSSIM | 0.745 | 0.903 | 0.935 | 0.958 | 0.955 | 0.976 | **0.979** |
| MSA | 20.57 | 10.45 | 8.285 | 7.202 | 7.992 | 5.598 | **4.485** |
| Time/s | - | 301.1 | 423.3 | 521.7 | 180.1 | 551.6 | **7.4** |
| ***Case 4: Gaussian noise + dead lines*** | | | | | | | |
| MPSNR | 21.91 | 25.94 | 27.49 | 31.31 | 32.06 | 30.65 | **33.86** |
| MSSIM | 0.752 | 0.908 | 0.931 | 0.967 | 0.965 | 0.971 | **0.979** |
| MSA | 20.25 | 10.063 | 5.712 | 5.732 | 6.583 | 6.041 | **4.595** |
| Time/s | - | 304.9 | 477.7 | 478.8 | 182.6 | 555.2 | **7.3** |
| ***Case 5.1: Gaussian noise + stripe noise + dead lines (SNR = 8dB)*** | | | | | | | |
| MPSNR | 21.36 | 25.63 | 27.28 | 30.79 | 31.34 | 30.29 | **32.69** |
| MSSIM | 0.735 | 0.898 | 0.927 | 0.950 | 0.948 | 0.959 | **0.975** |
| MSA | 22.34 | 10.81 | 5.857 | 7.998 | 8.209 | 7.083 | **4.681** |
| Time/s | - | 315.6 | 452.9 | 532.1 | 167.2 | 545.4 | **7.4** |
| ***Case 5.2: Gaussian noise + stripe noise + dead lines (SNR = 18dB)*** | | | | | | | |
| MPSNR | 24.15 | 28.03 | 31.48 | 33.57 | 33.63 | 34.25 | **35.14** |
| MSSIM | 0.782 | 0.937 | 0.965 | 0.974 | 0.979 | 0.982 | **0.985** |
| MSA | 17.63 | 8.145 | 4.873 | 4.465 | 5.156 | 4.367 | **4.186** |
| Time/s | - | 302.6 | 466.7 | 515.3 | 178.4 | 558.3 | **7.4** |
| ***Case 5.3: Gaussian noise + stripe noise + dead lines (SNR = 28dB)*** | | | | | | | |
| MPSNR | 31.86 | 33.68 | 34.37 | 38.48 | 37.96 | 40.36 | **40.65** |
| MSSIM | 0.937 | 0.956 | 0.964 | 0.981 | 0.978 | 0.989 | **0.991** |
| MSA | 7.842 | 6.543 | 6.468 | 5.347 | 5.357 | 3.975 | **3.458** |
| Time/s | - | 308.5 | 455.3 | 507.4 | 179.5 | 573.7 | **7.5** |
| ***Case 5.4: Gaussian noise + stripe noise + dead lines (SNR = 38dB)*** | | | | | | | |
| MPSNR | 39.16 | 40.12 | 41.07 | 43.56 | 43.26 | **45.98** | 45.36 |
| MSSIM | 0.974 | 0.979 | 0.982 | 0.991 | 0.990 | **0.994** | 0.993 |
| MSA | 4.635 | 4.561 | 4.246 | 3.378 | 3.424 | 3.175 | **2.894** |
| Time/s | - | 313.8 | 464.3 | 497.5 | 169.7 | 546.4 | **7.3** |

*Case* 2 *(Stripe Noise)*: A part of the bands in the HSIs were corrupted by stripe noise. In our experiments, ten bands of the original data were imposed with simulated stripe noise [41], [42]. The simulated stripe strategy is that we randomly select some rows in original bands. Half of these rows is integrally aggrandized with the strength of mean, and the remaining half is reduced with the strength of mean.

*Case* 3 *(Gaussian Noise + Stripe Noise)*: All bands in the HSIs were corrupted by Gaussian noise and some of the bands were corrupted by stripe noise. The Gaussian noise intensity and stripe noise were identical to Case 1 and Case 2, respectively.

*Case* 4 *(Gaussian Noise + Dead Lines)*: All the bands in the HSIs were corrupted by Gaussian noise and some of the bands were corrupted by dead lines. In our experiments, 20 bands of the original data were imposed with dead lines. The Gaussian noise intensity was identical to Case 1.

*Case* 5 *(Gaussian Noise + Stripe Noise + Dead Lines)*: All the bands in the HSIs were corrupted by Gaussian noise, and some of the bands were corrupted by dead lines and

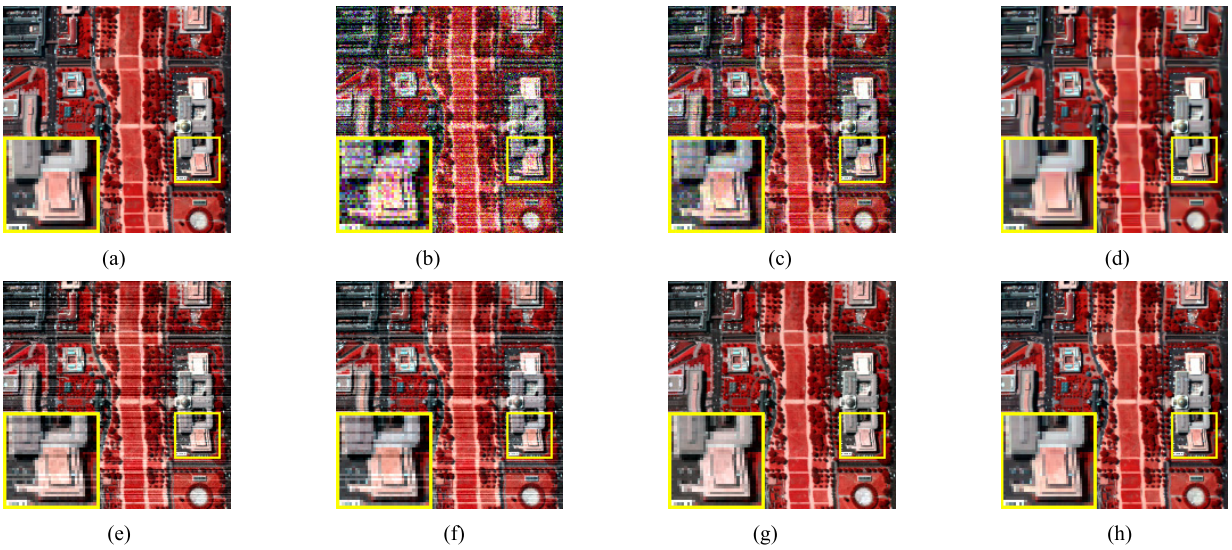


Fig. 6. Case 3. (a) Pseudo-color original image with bands (57, 27, 17). (b) Noisy image. (c) HSSNR. (d) BM4-D. (e) LRMR. (f) LRTV. (g) NonLRMA. (h) SSGN.

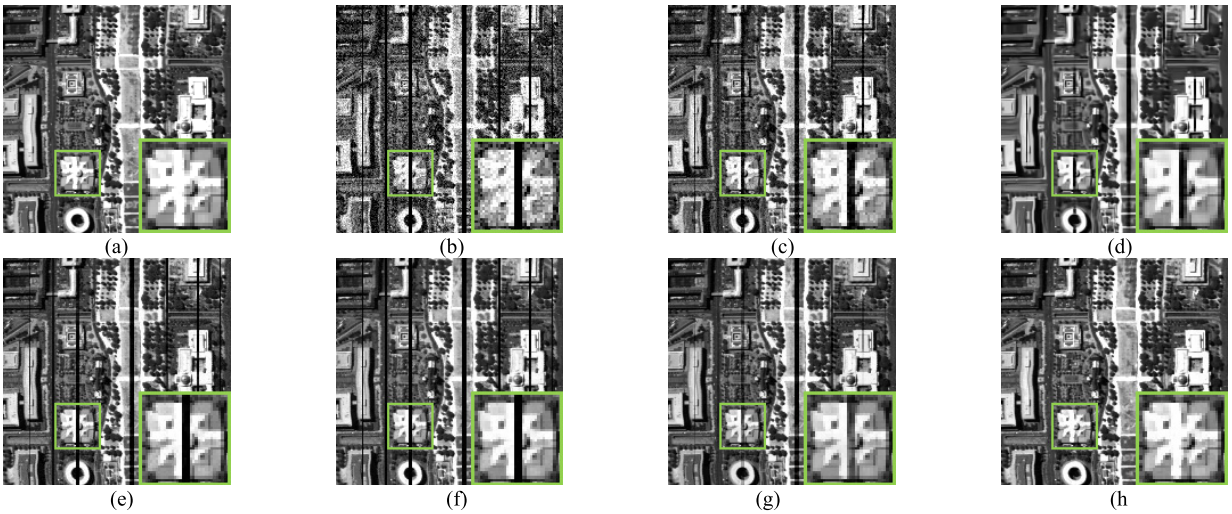


Fig. 7. Case 4. (a) Original image with band 164. (b) Noisy image. (c) HSSNR. (d) BM4-D. (e) LRMR. (f) LRTV. (g) NonLRMA. (h) SSGN.

stripe noise. Depending on the SNR, this case is divided into four levels (Cases 5.1–5.4). In Case 5.1 (SNR = 8 dB), the Gaussian noise intensity, stripes, and dead lines were identical to Case 1, Case 2, and Case 4, respectively. In addition, the SNR values of Cases 5.2, 5.3, and 5.4 gradually rise with 18-, 28-, and 38-dB simulated scenarios, respectively.

To acquire an integrated comparison for the other methods and the proposed SSGN, quantitative evaluation indices (MPSNR, MSSIM, and MSA) [43], [44], a visual comparison, curves of the spectra, and the spectral difference results were used to analyze the results of different methods. The average evaluation indices of the five cases with mixed noise are listed in Table I. To give detailed contrasting results, Cases 3–5.1 are chosen to demonstrate the visual results, corresponding to Figs. 6–8, respectively. Due to a large number of bands in an HSI, only a few bands are selected to give the visual results in each case with pseudo-color or gray color. Fig. 6 shows the denoising results of the different algorithms in simulated Case 3 with the pseudo-color view of bands 17, 27, and 57 (see enlarged details in the left corner of Fig. 6); Fig. 7 gives the denoising results of different algorithms in simulated Case 4 (see enlarged details in the right corner of Fig. 7); Fig. 8 shows the denoising results of different algorithms in simulated Case 5.1. The values of the PSNR and SSIM within different bands of the restored HSI in Cases 3–5.1 are depicted to assess the per-band denoising result in Fig. 9.

In Table I, the best performance for each quality index is marked in bold. Compared with the other algorithms, the proposed SSGN model achieves the highest MPSNR and MSSIM values and the lowest MSA values in all the simulated Cases 1–5.3, in addition to showing a preferable visual quality in Figs. 6–8. Although the HSSNR algorithm has an effective noise reduction ability under weak noise levels, as shown in Table I for Case 3, it cannot deal well with degraded bands with strong Gaussian noise, and the results still contain obvious residual noise, especially in Fig. 7. Furthermore, the stripes and dead lines are also not removed in Cases 3–5.1 through HSSNR. From Table I, BM4-D shows favorable noise

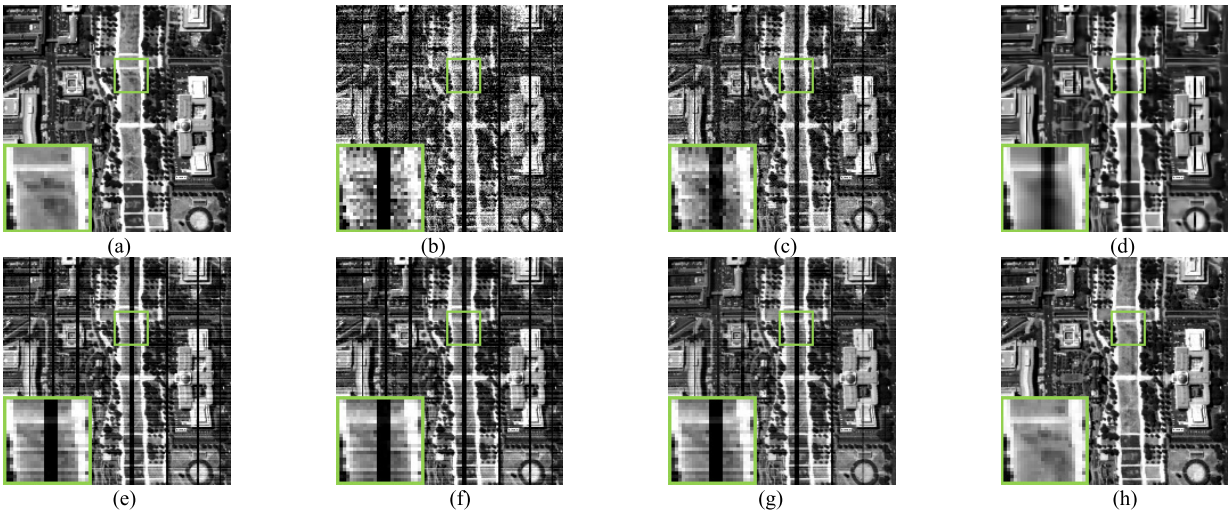


Fig. 8. Case 5.1. (a) Original image with band 54. (b) Noisy image. (c) HSSNR. (d) BM4-D. (e) LRMR. (f) LRTV. (g) NonLRMA. (h) SSGN.

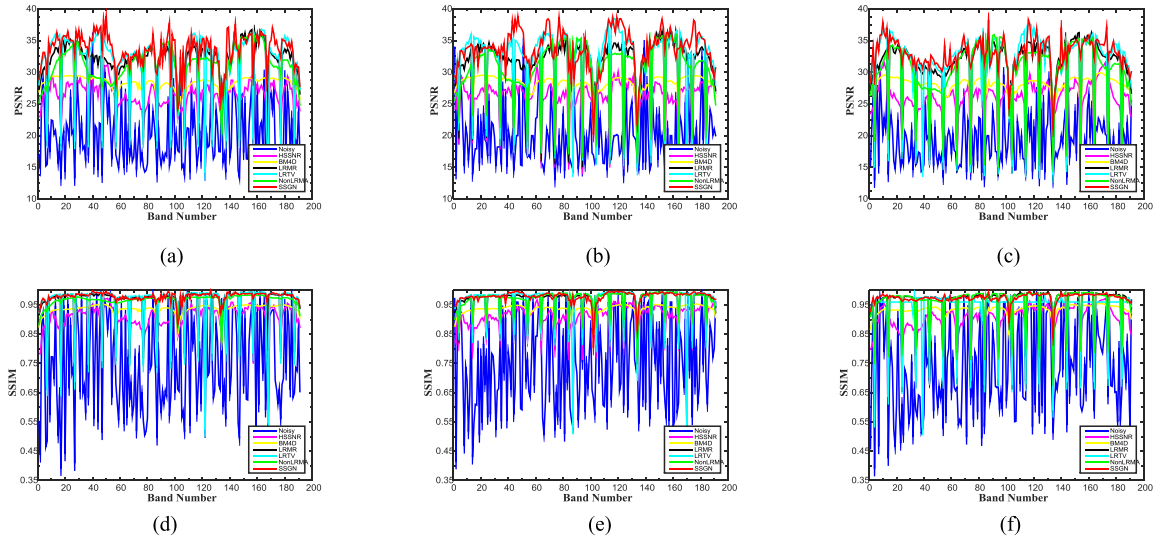


Fig. 9. (a)–(c) PSNR and (d)–(f) SSIM values of different denoising methods in each band of the simulated experiments with Cases 3, 4, and 5.1.

reduction ability under the nonuniform noise intensities for different bands. However, it also produces over-smoothing in the results in Figs. 6–8, since different nonlocal similar cubes in the HSI may result in the removal of small texture features. Exploring the low-rank property in spatial or spectral domain of the HSI, LRMR, LRTV, and NonLRMA provides favorable denoising results in Figs. 6–8 and Case 5.4 with high-level SNR value, respectively. However, there are still stripes, spectral distortion, and dead lines in the magnified areas, especially for the mixed noise, as in Fig. 8, due to the complexity of the mixed noise model in HSIs.

*Parameter Sensitivity Analysis*: The penalty parameter $\alpha$ for the tradeoff between the spatial and spectral items in (7) is critical in the HSI denoising procedure. To explore the influence of $\alpha$ for SSGN, Fig. 10 reveals the quantitative evaluation results (MPSNR and MSA) with different penalty values in the simulated experiments (Cases 1–3). In Case 1 with only Gaussian noise, the spatial loss function without the spectral item outperforms slightly than the spatial–spectral loss function in the MPSNR results, as shown in Fig. 10(a).

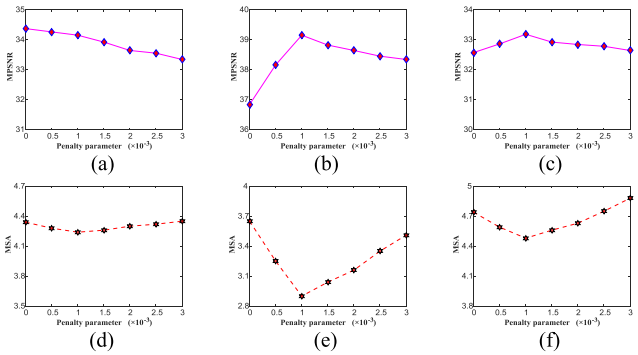


Fig. 10. Quantitative evaluation results under different values of $\alpha$. (a) mPSNR in Case 1. (b) mPSNR in Case 2. (c) mPSNR in Case 3. (d) MSA in Case 1. (e) MSA in Case 2. (f) MSA in Case 3.

The reason may be that the random noise can be effectively described and restrained through just mean square error (MSE) loss. Meanwhile, in case 2 and case 3 with mixed noise, especially sparse noise, from the perspective of spatial information

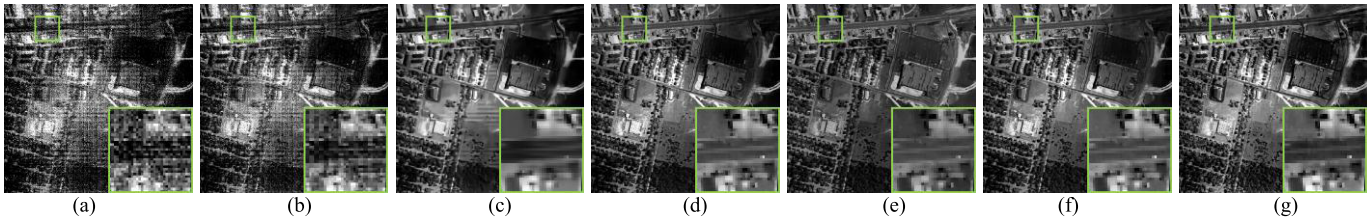


Fig. 11. Denoising results for the HYDICE Urban image. (a) Noisy image band 104. (b) HSSNR. (c) BM4-D. (d) LRMR. (e) LRTV. (f) NonLRMA. (g) SSGN.

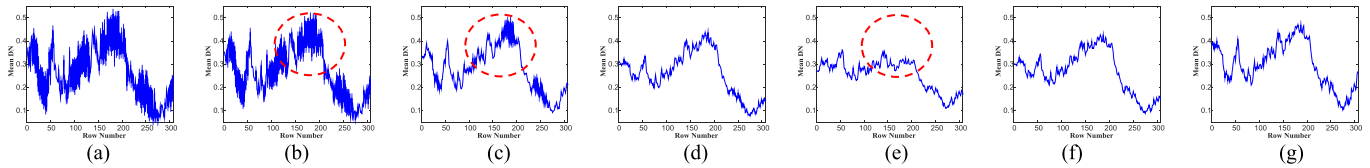


Fig. 12. Horizontal mean DN profiles of band 104 in Urban data set. (a) Noisy image. (b) HSSNR. (c) BM4-D. (d) LRMR. (e) LRTV. (f) NonLRMA. (g) SSGN.

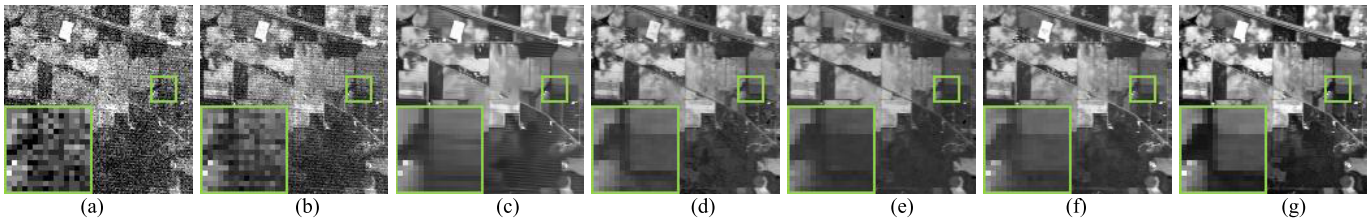


Fig. 13. Denoising results for the AVIRIS Indian Pines image. (a) Noisy image band 2. (b) HSSNR. (c) BM4-D. (d) LRMR. (e) LRTV. (f) NonLRMA. (g) SSGN.

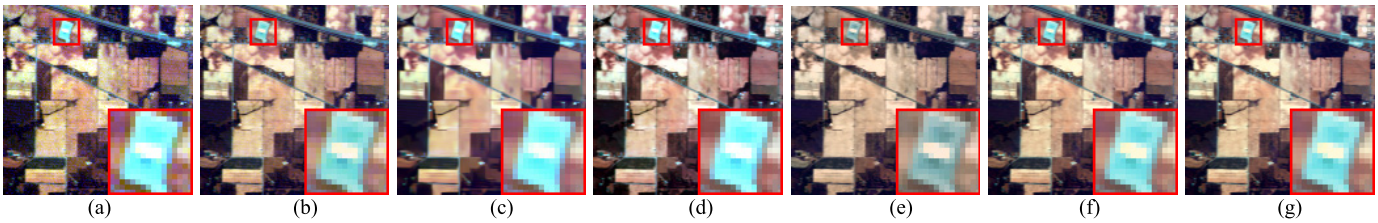


Fig. 14. Denoising results for the Indian Pines image. (a) Noisy image bands (145, 24, 2). (b) HSSNR. (c) BM4-D. (d) LRMR. (e) LRTV. (f) NonLRMA. (g) SSGN.

restoration, the MPSNR results of the proposed SSGN first rise with the increase of $\alpha$, as shown in Fig. 10 under the stripe or mixed noise scenario, and when the value is equal to 0.001, the results reach the highest MPSNR value. The results then gradually decrease with the increase of $\alpha$. From the other perspective of spectral information restoration, the MSA results of the proposed SSGN first decrease with the increase of $\alpha$, as shown in Fig. 10(d)–(f), and when the value is equal to 0.001, the results reach the lowest MSA value. The spectral distortion then gradually rises with the increase of $\alpha$. Essentially, the spectral preservation strategy is crucial for HSI denoising [45], [46] and can simultaneously maintain the spatial structure information and restrain the spectral distortion, especially for sparse noise.

### *B. Real-Data Experiments*

To further test the effectiveness of the proposed SSGN method for HSI mixed noise removal, three real-world HSI data sets, as shown in Figs. 11, 13, and 16, were employed in the real-data experiments. The original and restored mean normalized DN curves, in per-row or column form, through different methods are given in Figs. 12, 15, and 17, respectively.

1) *HYDICE Urban Data Set:* The noise types are mainly dense noise, stripe noise, and mixed noise of these two types. Fig. 11 displays the denoising results in band number 104 for the five comparing algorithms and the proposed SSGN model, respectively. For a more elaborate comparison, the original and restored mean normalized DN curves, in per-row form, through different algorithms are shown in Fig. 12.

   In Fig. 11, it can be clearly observed that HSSNR can reduce some of the noise, but the mixed noise still remains in the restored results. BM4-D does well in suppressing mixed noise, but it also introduces over-smoothing in some regions and loses many

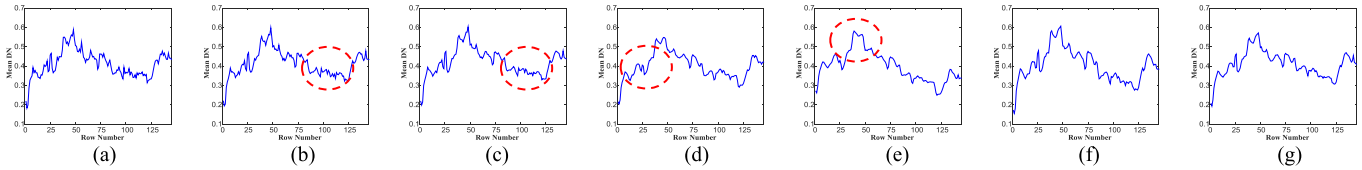


Fig. 15. Horizontal mean DN profiles of band 2 in Indian data set. (a) Noisy image. (b) HSSNR. (c) BM4-D. (d) LRMR. (e) LRTV. (f) NonLRMA. (g) SSGN.

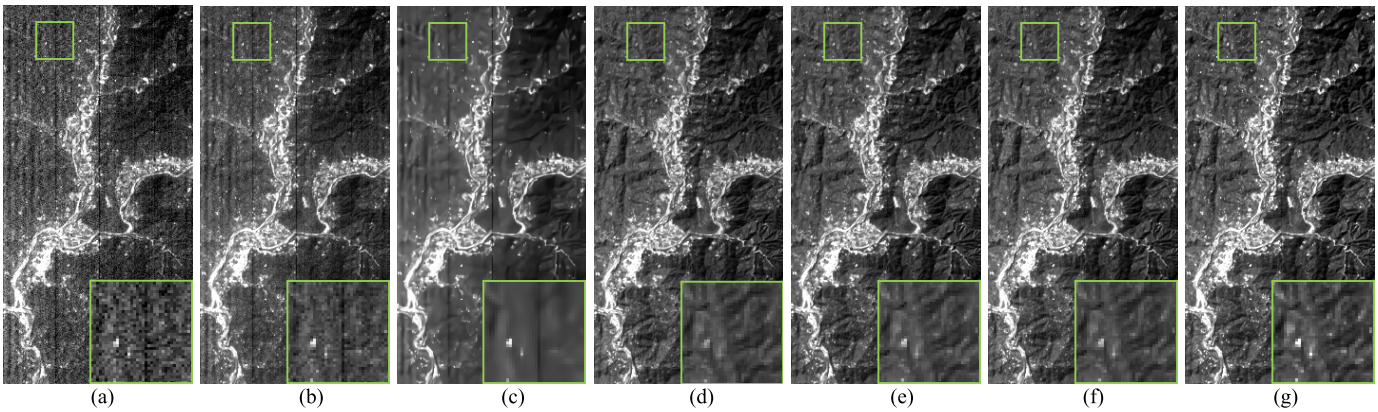


Fig. 16. Denoising results for the Hyperion EO-1 image. (a) Noisy image band 2. (b) HSSNR. (c) BM4-D. (d) LRMR. (e) LRTV. (f) NonLRMA. (g) SSGN.

high-frequency details due to the NLM strategy. LRMR, LRTV, and NonLRMA all perform well for mixed noise reduction, but they cannot preserve the spectral information well, as shown in Fig. 12. In contrast, SSGN performs the best in Figs. 11(g) and 12(g), effectively removing the mixed noise, while simultaneously preserving the local details, without introducing obvious over-smoothing or spectral distortion.

2) *AVIRIS Indian Pines Data Set:* The first few bands and several of the middle bands of the Indian Pines HSI are seriously corrupted by Gaussian noise and impulse noise. Figs. 13 and 14 show the denoising results of different methods, which represent band number 2 and bands (145, 24, 2) of the Indian Pines image, respectively. In Fig. 13, it can be clearly noticed that Gaussian noise and impulse noise still remain in the reconstructed results through HSSNR. BM4-D does well in reducing the dense noise, but it appears to be virtually powerless against heavy impulse noise. LRMR and NonLRMA perform well in reducing mixed noise. However, their restored results still exhibit obvious residual noise and stripes. The LRTV method also shows the ability of noise suppression, but some detailed information is simultaneously smoothed and destroyed in Fig. 14(e). SSGN exhibits the best performance for not only effectively removing the dense noise and impulse noise, but also simultaneously preserving the high-frequency details and structural information of the Indian Pines image both in Figs. 13–15.

3) *Hyperion EO-1 Data Set:* The first and last few bands of the EO-1 are seriously corrupted by Gaussian noise, stripe noise, and dead lines. Fig. 16, including partial enlarged details, shows the denoising results in band number 2 for five contrast algorithms, and the proposed SSGN, respectively. For a clearer comparison among these methods, the original and restored mean DN curves in per-column through different algorithms are displayed in Fig. 17, respectively.

In Fig. 16, it can be clearly observed that HSSNR can reduce some of the noise, but the mixed noise still remains in the restored results. BM4-D does well in suppressing dense noise, but it also introduces over-smoothing in most regions and loses much of the detailed information, by reason of the NLM strategy. LRMR, LRTV, and NonLRMA perform well for mixed noise reduction, but they cannot integrally recover the dead lines, as shown in Fig. 17 and the magnified results in Fig. 16. Outperforming all of the comparison methods, SSGN effectively reduces the mixed noise, while simultaneously preserves the local details and structural information, without bringing obvious over-smoothing effects or spectral distortions.

### C. Discussion

1) *Classification Validation*: To further validate the effect of the presented model, the classification results of the Indian Pines image before and after denoising are listed in Fig. 18 with different methods. Support vector machine (SVM) was utilized as the classifier under the same environment for all the restoration results. The overall accuracy (OA) and the kappa coefficient are given as evaluation indexes in Table II. SSGN performs better with the highest OA and kappa indexes of 85.4% and 0.831, respectively. This also verifies the effectiveness of the proposed HSI denoising method.

2) *Run-Time Comparison*: To compare the work efficiency of different denoising algorithms, the average running

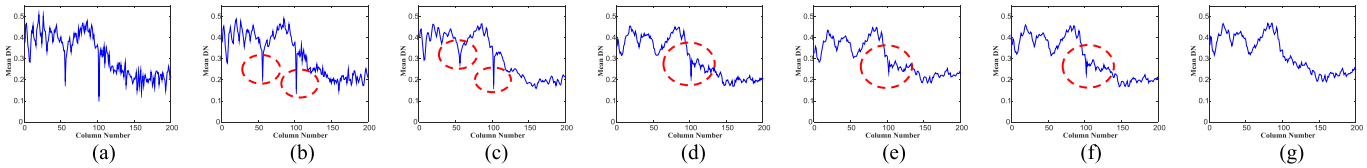


Fig. 17. Vertical mean DN profiles of band 2 in Hyperion EO-1 data set. (a) Noisy image. (b) HSSNR. (c) BM4-D. (d) LRMR. (e) LRTV. (f) NonLRMA. (g) SSGN.

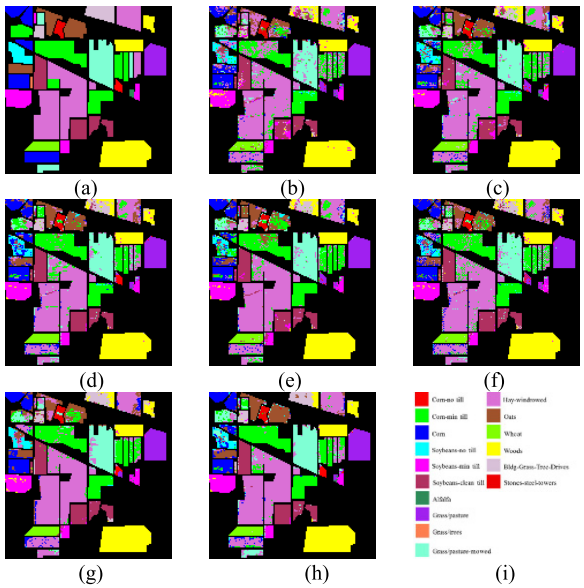


Fig. 18. Classification results for the Indian Pines image. (a) Noisy image. (b) HSSNR. (c) BM4-D. (d) LRMR. (e) LRTV. (f) NonLRMA. (g) SSGN. (g) NonLRMA. (h) SSGN. (i) 16 classes.

TABLE II
CLASSIFICATION ACCURACY RESULTS FOR INDIAN PINES

| | Original | HSSNR | BM4D | LRMR | LRTV | NonLRMA | SSGN |
|---|---|---|---|---|---|---|---|
| OA | 75.9% | 78.7% | 83.9% | 79.4% | 80.5% | 84.7% | **85.4%** |
| Kappa | 0.722 | 0.743 | 0.816 | 0.764 | 0.789 | 0.824 | **0.831** |

times were recorded for the three real-data experiments under the same operational environment (Software: Windows 7, MATLAB R2014b, CUDA 8.0; Hardware: 16-GB RAM, E5-2609v3 CPU, GTX TITAN X GPU), as listed in Table III. Clearly, the proposed SSGN shows the lowest run-time consumption, due to the high efficiency of this unified learning framework under GPU mode.

3) *Overall Evaluation*: Compared with the other existing HSI denoising algorithms in both simulated and actual experiments, SSGN outperforms in most evaluation indices (as listed in Table I), visual assessments (as shown in Figs. 11–17), classification accuracy (as listed in Table II), and time consumption (as listed in Table III), under different mixed noise scenarios. Although the existing HSI denoising methods can obtain favorable results, the inadaptability for hybrid noise removal in different HSIs and the low-efficiency issue still restrict the application of HSI denoising. The significant advantage of the proposed model is that SSGN can efficiently deal with multiple types of scenarios, without manually adjusting presupposed parameters through the data-driven mode. Nevertheless, the limitations of the proposed SSGN still exist, such as more complex types of dense-distributed strip noise and independent band normalization problems.

TABLE III
RUN-TIME COMPARISON FOR THE REAL-DATA EXPERIMENTS (SECONDS)

| Dataset | HSSNR | BM4D | LRMR | LRTV | NonLRMA | SSGN |
|---|---|---|---|---|---|---|
| Urban | 594.6 | 923.1 | 1147.8 | 385.2 | 1264.3 | **15.6** |
| Indian | 162.7 | 236.3 | 268.7 | 102.4 | 314.8 | **3.9** |
| EO-1 | 486.5 | 812.7 | 936.3 | 317.8 | 972.4 | **11.5** |

## V. CONCLUSION

In this paper, we present an SSGN for hybrid noise reduction in HSIs considering the noise type of Gaussian noise, stripe noise, impulse noise, dead line, and their mixture. In future works, we will combine more prior characteristics in HSIs with the data-driven learning framework, such as the low-rank tensor factorization model, to effectively utilize the characteristics of HSIs. In addition, holistic bands normalization strategy should be developed for better utilizing redundancy and highly correlated spectral information in HSI denoising task.

## REFERENCES

[1] X. Lu, W. Zhang, and X. Li, "A hybrid sparsity and distance-based discrimination detector for hyperspectral images," *IEEE Trans. Geosci. Remote Sens.*, vol. 56, no. 3, pp. 1703–1717, Mar. 2018.
[2] Y. Xu, L. Zhang, B. Du, and F. Zhang, "Spectral–spatial unified networks for hyperspectral image classification," *IEEE Trans. Geosci. Remote Sens.*, vol. 56, no. 10, pp. 5809–5893, Oct. 2018.
[3] X. Lu, H. Wu, and Y. Yuan, "Double constrained NMF for hyperspectral unmixing," *IEEE Trans. Geosci. Remote Sens.*, vol. 52, no. 5, pp. 2746–2758, May 2014.
[4] X. Lu, H. Wu, Y. Yuan, P. Yan, and X. Li, "Manifold regularized sparse NMF for hyperspectral unmixing," *IEEE Trans. Geosci. Remote Sens.*, vol. 51, no. 5, pp. 2815–2826, May 2013.
[5] B. Rasti, P. Scheunders, P. Ghamisi, G. Licciardi, and J. Chanussot, "Noise reduction in hyperspectral imagery: Overview and application," *Remote Sens.*, vol. 10, no. 3, p. 482, 2018.
[6] X. Lu, Y. Wang, and Y. Yuan, "Graph-regularized low-rank representation for destriping of hyperspectral images," *IEEE Trans. Geosci. Remote Sens.*, vol. 51, no. 7, pp. 4009–4018, Jul. 2013.
[7] L. Yan, R. Zhu, Y. Liu, and N. Mo, "Scene capture and selected codebook-based refined fuzzy classification of large high-resolution images," *IEEE Trans. Geosci. Remote Sens.*, vol. 56, no. 7, pp. 4178–4192, Jul. 2018.
[8] H. Othman and S.-E. Qian, "Noise reduction of hyperspectral imagery using hybrid spatial-spectral derivative-domain wavelet shrinkage," *IEEE Trans. Geosci. Remote Sens.*, vol. 44, no. 2, pp. 397–408, Feb. 2006.
[9] M. Maggioni, V. Katkovnik, K. Egiazarian, and A. Foi, "Nonlocal transform-domain filter for volumetric data denoising and reconstruction," *IEEE Trans. Image Process.*, vol. 22, no. 1, pp. 119–133, Jan. 2012.

[10] Q. Yuan, L. Zhang, and H. Shen, "Hyperspectral image denoising employing a spectral–spatial adaptive total variation model," *IEEE Trans. Geosci. Remote Sens.*, vol. 50, no. 10, pp. 3660–3677, Oct. 2012.
[11] Y.-Q. Zhao and J. Yang, "Hyperspectral image denoising via sparse representation and low-rank constraint," *IEEE Trans. Geosci. Remote Sens.*, vol. 53, no. 1, pp. 296–308, Jan. 2015.
[12] J. Li, Q. Yuan, H. Shen, and L. Zhang, "Noise removal from hyperspectral image with joint spectral-spatial distributed sparse representation," *IEEE Trans. Geosci. Remote Sens.*, vol. 54, no. 9, pp. 5425–5439, Jun. 2016.
[13] H. Zhang, W. He, L. Zhang, H. Shen, and Q. Yuan, "Hyperspectral image restoration using low-rank matrix recovery," *IEEE Trans. Geosci. Remote Sens.*, vol. 52, no. 8, pp. 4729–4743, Aug. 2014.
[14] W. He, H. Zhang, L. Zhang, and H. Shen, "Total-variation-regularized low-rank matrix factorization for hyperspectral image restoration," *IEEE Trans. Geosci. Remote Sens.*, vol. 54, no. 1, pp. 178–188, Jan. 2016.
[15] H. Fan, C. Li, Y. Guo, G. Kuang, and J. Ma, "Spatial–spectral total variation regularized low-rank tensor decomposition for hyperspectral image denoising," *IEEE Trans. Geosci. Remote Sens.*, vol. 56, no. 10, pp. 6196–6213, Oct. 2018.
[16] Q. Xie, Q. Zhao, D. Meng, and Z. Xu, "Kronecker-basis-representation based tensor sparsity and its applications to tensor recovery," *IEEE Trans. Pattern Anal. Mach. Intell.*, vol. 40, no. 8, pp. 1888–1902, Aug. 2017.
[17] Y. Chen, X. Cao, Q. Zhao, D. Meng, and Z. Xu, "Denoising hyperspectral image with non-i.i.d. noise structure," *IEEE Trans. Cybern.*, vol. 48, no. 3, pp. 1054–1066, Mar. 2018.
[18] Y. LeCun, Y. Bengio, and G. Hinton, "Deep learning," *Nature*, vol. 521, pp. 436–444, May 2015.
[19] Y. LeCun *et al.*, "Handwritten digit recognition with a back-propagation network," in *Proc. Adv. Neural Inf. Process. Syst.*, 1990, pp. 396–404.
[20] Q. Zhang, Q. Yuan, J. Li, Z. Yang, and X. Ma, "Learning a dilated residual network for SAR image despeckling," *Remote Sens.*, vol. 10, no. 2, p. 196, 2018.
[21] Y. Wei, Q. Yuan, H. Shen, and L. Zhang, "Boosting the accuracy of multispectral image pansharpening by learning a deep residual network," *IEEE Geosci. Remote Sens. Lett.*, vol. 14, no. 10, pp. 1795–1799, Oct. 2017.
[22] G. Scarpa, S. Vitale, and D. Cozzolino, "Target-adaptive CNN-based pansharpening," *IEEE Trans. Geosci. Remote Sens.*, vol. 56, no. 9, pp. 5443–5457, Sep. 2018.
[23] Q. Zhang, Q. Yuan, C. Zeng, X. Li, and Y. Wei, "Missing data reconstruction in remote sensing image with a unified spatial–temporal–spectral deep convolutional neural network," *IEEE Trans. Geosci. Remote Sens.*, vol. 56, no. 8, pp. 4274–4288, Aug. 2018.
[24] Y. Qian and M. Ye, "Hyperspectral imagery restoration using nonlocal spectral-spatial structured sparse representation with noise estimation," *IEEE J. Sel. Topics Appl. Earth Observ. Remote Sens.*, vol. 6, no. 2, pp. 499–515, Apr. 2013.
[25] T. Lu, S. Li, L. Fang, Y. Ma, and J. A. Benediktsson, "Spectral–spatial adaptive sparse representation for hyperspectral image denoising," *IEEE Trans. Geosci. Remote Sens.*, vol. 54, no. 1, pp. 373–385, Jan. 2016.
[26] Q. Wang, L. Zhang, Q. Tong, and F. Zhang, "Hyperspectral imagery denoising based on oblique subspace projection," *IEEE J. Sel. Topics Appl. Earth Observ. Remote Sens.*, vol. 7, no. 6, pp. 2468–2480, Jun. 2014.
[27] K. Dabov, A. Foi, V. Katkovnik, and K. Egiazarian, "Image denoising by sparse 3-D transform-domain collaborative filtering," *IEEE Trans. Image Process.*, vol. 16, no. 8, pp. 2080–2095, Aug. 2007.
[28] L. Zhang, L. Zhang, and B. Du, "Deep learning for remote sensing data: A technical tutorial on the state of the Art," *IEEE Geosci. Remote Sens. Mag.*, vol. 4, no. 2, pp. 22–40, Jun. 2016.
[29] X. X. Zhu *et al.*, "Deep learning in remote sensing: A comprehensive review and list of resources," *IEEE Geosci. Remote Sens. Mag.*, vol. 5, no. 4, pp. 8–36, Dec. 2017.
[30] G.-S. Xia *et al.*, "AID: A benchmark data set for performance evaluation of aerial scene classification," *IEEE Trans. Geosci. Remote Sens.*, vol. 55, no. 7, pp. 3965–3981, Jul. 2017.
[31] X. Mao, C. Shen, and Y.-B. Yang, "Image restoration using very deep convolutional encoder-decoder networks with symmetric skip connections," in *Proc. NIPS*, 2016, pp. 2802–2810.
[32] K. Zhang, W. Zuo, Y. Chen, D. Meng, and L. Zhang, "Beyond a Gaussian Denoiser: Residual learning of deep CNN for image denoising," *IEEE Trans. Image Process.*, vol. 26, no. 7, pp. 3142–3155, Jul. 2017.
[33] K. He, X. Zhang, S. Ren, and J. Sun, "Deep residual learning for image recognition," in *Proc. IEEE Conf. Comput. Vis. Pattern Recognit.*, Jun. 2016, pp. 770–778.
[34] Y. Chen, Y. Guo, Y. Wang, D. Wang, C. Peng, and G. He, "Denoising of hyperspectral images using nonconvex low rank matrix approximation," *IEEE Trans. Geosci. Remote Sens.*, vol. 55, no. 9, pp. 5366–5380, Sep. 2017.
[35] X. Liu, H. Shen, Q. Yuan, X. Lu, and C. Zhou, "A universal destriping framework combining 1-D and 2-D variational optimization methods," *IEEE Trans. Geosci. Remote Sens.*, vol. 56, no. 2, pp. 808–822, Feb. 2018.
[36] Q. Yuan, Q. Zhang, J. Li, H. Shen, and L. Zhang, "Hyperspectral image denoising employing a spatial–spectral deep residual convolutional neural network," *IEEE Trans. Geosci. Remote Sens.*, vol. 57, no. 2, pp. 1205–1218, Feb. 2019.
[37] Q. Wang *et al.*, "Fusion of Landsat 8 OLI and sentinel-2 MSI data," *IEEE Trans. Geosci. Remote Sens.*, vol. 55, no. 7, pp. 3885–3899, Jul. 2017.
[38] D. Kingma and J. Ba. (2014). "Adam: A method for stochastic optimization." [Online]. Available: https://arxiv.org/abs/1412.6980
[39] Y. Jia *et al.*, "Caffe: Convolutional architecture for fast feature embedding," in *Proc. ACM Int. Conf. Multimedia*, 2014, pp. 675–678.
[40] W. Xie and Y. Li, "Hyperspectral imagery denoising by deep learning with trainable nonlinearity function," *IEEE Geosci. Remote Sens. Lett.*, vol. 14, no. 11, pp. 1963–1967, Nov. 2017.
[41] X. Liu, X. Lu, H. Shen, Q. Yuan, Y. Jiao, and L. Zhang, "Stripe noise separation and removal in remote sensing images by consideration of the global sparsity and local variational properties," *IEEE Trans. Geosci. Remote Sens.*, vol. 54, no. 5, pp. 3049–3060, May 2016.
[42] Y. Chang, L. Yan, H. Fang, and C. Luo, "Anisotropic spectral-spatial total variation model for multispectral remote sensing image destriping," *IEEE Trans. Image Process.*, vol. 24, no. 6, pp. 1852–1866, Jun. 2015.
[43] C. Yi, Y.-Q. Zhao, and J. C.-W. Chan, "Hyperspectral image super-resolution based on spatial and spectral correlation fusion," *IEEE Trans. Geosci. Remote Sens.*, vol. 56, no. 7, pp. 4165–4177, Jul. 2018.
[44] H. Shen, X. Meng, and L. Zhang, "An integrated framework for the spatio–temporal–spectral fusion of remote sensing images," *IEEE Trans. Geosci. Remote Sens.*, vol. 54, no. 12, pp. 7135–7148, Dec. 2016.
[45] Q. Tong, Y. Xue, and L. Zhang, "Progress in hyperspectral remote sensing science and technology in China over the past three decades," *IEEE J. Sel. Topics Appl. Earth Observ. Remote Sens.*, vol. 7, no. 1, pp. 70–91, Jan. 2014.
[46] J. Xue, Y. Zhao, W. Liao, and S. G. Kong, "Joint spatial and spectral low-rank regularization for hyperspectral image denoising," *IEEE Trans. Geosci. Remote Sens.*, vol. 56, no. 4, pp. 1940–1958, Apr. 2018.

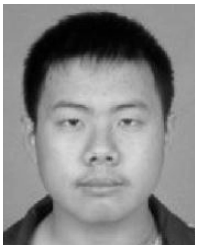

**Qiang Zhang** (S'17) received the B.S. degree in surveying and mapping engineering and the M.S. degree in photogrammetry and remote sensing from Wuhan University, Wuhan, China, in 2017 and 2019, respectively, where he is currently pursuing the Ph.D. degree with the State Key Laboratory of Information Engineering in Surveying, Mapping, and Remote Sensing.

His research interests include image quality improvement, data fusion, deep learning, and computer vision.

**Qiangqiang Yuan** (M'13) received the B.S. degree in surveying and mapping engineering and the Ph.D. degree in photogrammetry and remote sensing from Wuhan University, Wuhan, China, in 2006 and 2012, respectively.

In 2012, he joined the School of Geodesy and Geomatics, Wuhan University, where he is currently a Professor. He has authored more than 60 research papers, including more than 40 peer-reviewed articles in international journals such as the IEEE TRANSACTIONS ON IMAGE PROCESSING and the IEEE TRANSACTIONS ON GEOSCIENCE AND REMOTE SENSING. His research interests include image reconstruction, remote sensing image processing and application, and data fusion.

Dr. Yuan was a recipient of the Top-Ten Academic Star of Wuhan University in 2011 and the Hong Kong Scholar Award from the Society of Hong Kong Scholars and the China National Postdoctoral Council, in 2014. He has frequently served as a referee for more than 20 international journals for remote sensing and image processing. He is currently serving as an Associate Editor for the IEEE ACCESS.

**Jie Li** (M'16) received the B.S. degree in sciences and techniques of remote sensing and the Ph.D. degree in photogrammetry and remote sensing from Wuhan University, Wuhan, China, in 2011 and 2016, respectively.

He is currently a Lecturer with the School of Geodesy and Geomatics, Wuhan University. His research interests include image quality improvement, super-resolution, data fusion, remote sensing image processing, sparse representation, and deep learning.

**Xinxin Liu** received the B.S. degree in geographic information system and the Ph.D. degree in cartography and geographic information system from Wuhan University, Wuhan, China, in 2013 and 2018, respectively.

In 2018, she joined the College of Electrical and Information Engineering, Hunan University, Changsha, China, where she is currently an Assistant Professor. Her research interests include image quality improvement, remote sensing image processing, and remote sensing mapping and application.

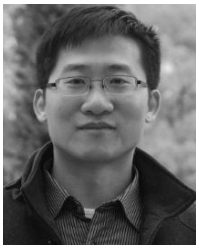

**Huanfeng Shen** (M'10–SM'13) received the B.S. degree in surveying and mapping engineering and the Ph.D. degree in photogrammetry and remote sensing from Wuhan University, Wuhan, China, in 2002 and 2007, respectively.

In 2007, he joined the School of Resource and Environmental Sciences, Wuhan University, where he is currently a Luojia Distinguished Professor. He has been supported by several talent programs, such as the Youth Talent Support Program of China in 2015, the China National Science Fund for Excellent Young Scholars in 2014, and the New Century Excellent Talents by the Ministry of Education of China in 2011. He has authored over 100 research papers. His research interests include image quality improvement, remote sensing mapping and application, data fusion and assimilation, and regional and global environmental changes.

Dr. Shen is currently a member of the Editorial Board of the *Journal of Applied Remote Sensing*.

**Liangpei Zhang** (M'06–SM'08–F'19) received the B.S. degree in physics from Hunan Normal University, Changsha, China, in 1982, the M.S. degree in optics from the Xi'an Institute of Optics and Precision Mechanics, Chinese Academy of Sciences, Xi'an, China, in 1988, and the Ph.D. degree in photogrammetry and remote sensing from Wuhan University, Wuhan, China, in 1998.

He was the Head of the Remote Sensing Division, State Key Laboratory of Information Engineering in Surveying, Mapping and Remote Sensing (LIESMARS), Wuhan University. He is also a "Chang-Jiang Scholar" Chair Professor appointed by the Ministry of Education of China. He is currently a Principal Scientist for the China State Key Basic Research Project (2011–2016) appointed by the Ministry of National Science and Technology of China to lead the Remote Sensing Program in China. He has authored more than 600 research papers and 7 books. He holds 15 patents. His research interests include hyperspectral remote sensing, high-resolution remote sensing, image processing, and artificial intelligence.

Dr. Zhang is a fellow of the Institution of Engineering and Technology (IET) and an Executive Member (Board of Governor) of the China National Committee of International Geosphere–Biosphere Programme and the China Society of Image and Graphics. He was a recipient of the 2010 Best Paper Boeing Award, the 2013 Best Paper ERDAS Award from the American Society of Photogrammetry and Remote Sensing (ASPRS), and the best reviewer awards from the IEEE Geoscience and Remote Sensing Society (GRSS) for his service to the IEEE JOURNAL OF SELECTED TOPICS IN EARTH OBSERVATIONS AND APPLIED REMOTE SENSING (JSTARS) in 2012 and the IEEE GEOSCIENCE AND REMOTE SENSING LETTERS (GRSL) in 2014. His research teams won the top three prizes of the IEEE GRSS 2014 Data Fusion Contest, and his students have been selected as the winners or finalists of the IEEE International Geoscience and Remote Sensing Symposium (IGARSS) Student Paper Contest in recent years. He is the Founding Chair of the IEEE GRSS Wuhan Chapter. He was the General Chair for the 4th IEEE GRSS Workshop on Hyperspectral Image and Signal Processing: Evolution in Remote Sensing (WHISPERS) and the Guest Editor of JSTARS. He regularly serves as a Co-Chair of the series SPIE conferences on multispectral image processing and pattern recognition, conference on Asia remote sensing, and many other conferences. He is the Editor of several conference proceedings, issues, and geoinformatics symposiums. He also serves as an Associate Editor for the*International Journal of Image and Graphic*s, the *International Journal of Digital Multimedia Broadcasting*, the *Journal of Geo-Spatial Information Science*, and the *Journal of Remote Sensing,* and the Guest Editor of the *Journal of Applied Remote Sensing* and the *Journal of Sensors.* He is currently serving as an Associate Editor for the IEEE TRANSACTIONS ON GEOSCIENCE AND REMOTE SENSING.